



# Integrating vacancy engineering and energy-level adapted coupling of electrocatalyst for enhancement of carbon dioxide conversion

Yi Li<sup>a,1</sup>, Weidong Niu<sup>a,1</sup>, Tao Chen<sup>c</sup>, Ye Sun<sup>b,\*</sup>, Miao Yu<sup>a,\*</sup>

<sup>a</sup> State Key Laboratory of Urban Water Resource and Environment, School of Chemistry and Chemical Engineering, Harbin Institute of Technology, Harbin 150001, China

<sup>b</sup> Condensed Matter Science and Technology Institute, School of Instrumentation Science and Engineering, Harbin Institute of Technology, Harbin 150001, China

<sup>c</sup> State Key Laboratory of Environment-friendly Energy Materials, Southwest University of Science and Technology, Mianyang 621010, China

## ARTICLE INFO

### Keywords:

CO<sub>2</sub> reduction reaction  
Chemical coupling  
Vacancy engineering  
Hybrid electrocatalyst  
Tin disulfide

## ABSTRACT

CO<sub>2</sub> activation capability and conductivity of electrocatalysts are two crucial factors to address the high activation barrier and slow kinetics of CO<sub>2</sub> reduction reaction (CO<sub>2</sub>RR). Still, substantial promotion of both factors remains challenging. Herein, we report sulfur-deficient tin disulfide covered nitrogen-doped hollow carbon spheres (SnS<sub>2-x</sub>/NHCS) as electrocatalyst for CO<sub>2</sub>RR. Combining experimental analysis with calculations, we demonstrate that the S vacancies and energy-level adapted coupling can decrease the reaction barrier, increase the CO<sub>2</sub> adsorption capacity and affinity with the intermediate, and promote the conductivity, delivering a current density of 35.3 mA cm<sup>-2</sup> at -1.2 V vs. reversible hydrogen electrode (RHE) and a Faradaic efficiency for formate > 80% in a large potential range from -0.8 to -1.2 V (vs. RHE). This work unravels the relationship of the vacancy engineering/hybrid coupling of SnS<sub>2-x</sub>/NHCS with its CO<sub>2</sub>RR performance, and proposes a convenient route to boost the CO<sub>2</sub> activation capability and conductivity of electrocatalysts simultaneously.

## 1. Introduction

Electrochemical reduction of carbon dioxide (CO<sub>2</sub>) to carbonaceous feedstock has been acknowledged to be a particularly promising approach to address the increasingly acute greenhouse effect and energy demands [1–4]. CO<sub>2</sub> is chemically inert with a low electron affinity which requires to overcome a substantial energy barrier (~750 kJ mol<sup>-1</sup>) to dissociate the C=O bond for CO<sub>2</sub> conversion [5]. Due to the high barrier for CO<sub>2</sub> activation and slow electron transfer kinetics, CO<sub>2</sub> reduction reaction (CO<sub>2</sub>RR) normally suffers from severe energy loss and high applied overpotential [6,7]. In this context, enhancing the CO<sub>2</sub> activation capability and conductivity of electrocatalysts have become two main strategies for CO<sub>2</sub>RR. For a given parent catalyst, the former is primarily based on promoting the amount and activity of active sites, which can be accomplished by introducing vacancies to the catalysts [8–11]. For example, oxygen (O) vacancies could offer the active sites to anchor the intermediate of CO<sub>2</sub>RR [12], and sulfur (S) vacancies allowed the consecutive reduction of CO<sub>2</sub> molecules on the catalyst surface [13,14]. For the latter strategy, given that conductivity is closely associated with surface carrier density, regulating the electronic

structure of the catalyst is an efficient path [15–17].

Constructing hybrid electrocatalysts based on chemical coupling between different components have demonstrated great promise to increase the current density during CO<sub>2</sub>RR [18–20]. For example, carbon nanotube was used as a conductive scaffold to support phthalocyanines, and their hybrid showed an enlarged electrochemically-active surface area and improved physical and chemical robustness [21]; carbon layer was found to increase the electrical conductivity via fine-tuning of the surface chemical and electronic structures [22]. So far, results on chemical coupling of the hybrid electrocatalysts have been primarily focused on their CO<sub>2</sub>RR performance, whilst the underlying mechanism about how chemical coupling between the components can promote the current density during CO<sub>2</sub>RR process has been inexplicit.

Herein, we report S-deficient tin disulfide coupled nitrogen-doped hollow carbon spheres (SnS<sub>2-x</sub>/NHCS) for CO<sub>2</sub>RR and the underlying mechanism for its enhanced performance compared with SnS<sub>2</sub>. Based on our density functional theory (DFT) calculations, S vacancies in SnS<sub>2-x</sub> and its coupling with the N-doped carbon can effectively regulate the charge distribution, introduce the active sites, modify the band structure near the Fermi level, and enable electron flow from the N-doped carbon

\* Corresponding authors.

E-mail addresses: [sunye@hit.edu.cn](mailto:sunye@hit.edu.cn) (Y. Sun), [miaoyu\\_che@hit.edu.cn](mailto:miaoyu_che@hit.edu.cn) (M. Yu).

<sup>1</sup> These authors contributed equally to this work.

to  $\text{SnS}_{2-x}$ . These variations can increase the adsorption of  $\text{CO}_2$ , strengthen the bonding of the intermediate ( $^*\text{OOCH}$ ) at the catalyst surface, meanwhile reduce the energy barrier for  $\text{CO}_2$  activation and accelerate the electron transfer kinetics. The measured carrier density of  $\text{SnS}_{2-x}/\text{NHCS}$  is 12.1 and 10.0 folds as that of  $\text{SnS}_2$  and  $\text{SnS}_{2-x}$ , respectively, meanwhile the electrical resistance is largely reduced. As a result, for electrochemical reduction of  $\text{CO}_2$ ,  $\text{SnS}_{2-x}/\text{NHCS}$  delivers a high geometrical current density of  $35.3 \text{ mA cm}^{-2}$  at  $-1.2 \text{ V}$  vs. reversible hydrogen electrode (RHE), together with high production selectivity and high operation durability. The  $\text{SnS}_{2-x}/\text{NHCS}$  delivers a current density of  $30.1 \text{ mA cm}^{-2}$  for formate at  $-1.2 \text{ V}$  (vs. RHE) and a Faradaic efficiency (FE)  $> 80\%$  for formate in a large potential range from  $-0.8$  to  $-1.2 \text{ V}$  (vs. RHE).

## 2. Experimental section

### 2.1. Calculation methods

The Vienna *ab initio* simulation package (VASP) was used to execute the DFT calculations. Heyd-Scuseria-Ernzerhof (HSE06) exchange-correlation density functional was employed to describe the electron properties in each calculation system. Monkhorst-Pack  $k$ -point was set to  $1 \times 1 \times 1$  for the structural optimization. The force convergence criterion used for the geometry relaxation was  $0.02 \text{ eV } \text{\AA}^{-1}$ . For the calculations of DOS and band structure, a plane-wave cutoff energy of  $400 \text{ eV}$  and Monkhorst-Pack  $k$ -point mesh of  $3 \times 3 \times 3$  in the Brillouin zone were sampled.

### 2.2. Chemicals and materials

Ammonia solution (25–28 %), tetraethyl orthosilicate (TEOS), dopamine hydrochloride, stannic chloride hydrated ( $\text{SnCl}_4 \cdot 0.5 \text{ H}_2\text{O}$ ), thioacetamide, ethanol (99.8 %), and hydrofluoric acid (HF, 40 %) were purchased from Aladdin Reagent Co., Ltd (Shanghai). Deionized (DI) water with a resistance value of  $\sim 18.25 \text{ M}\Omega \text{ cm}$  was used.

### 2.3. Synthesis of NHCS

The NHCS was synthesized according to the reported method with minor modification [23]. Typically, ethanol (10 mL) was mixed with ammonia (0.5 mL) and DI water (40 mL) in a beaker (100 mL) upon magnetic stirring for 20 min under ambient conditions. Then, TEOS (0.5 mL) was dropwise added into the mixture upon stirring for 10 min, followed by addition of aqueous solution of dopamine hydrochloride ( $40 \text{ mg mL}^{-1}$ , 5 mL) under continuous stirring for 24 h. The product ( $\text{SiO}_2/\text{dopamine}$ ) was collected by centrifugation and washed three times with DI water and ethanol. The as-prepared  $\text{SiO}_2/\text{dopamine}$  (100 mg) was placed in a quartz tube and heated to  $800^\circ\text{C}$  at a rate of  $5^\circ\text{C min}^{-1}$ , keeping in a nitrogen atmosphere for 4 h to obtain  $\text{SiO}_2/\text{NC}$ . The NHCS was finally acquired by etching the  $\text{SiO}_2/\text{NC}$  in HF (5%) for 2 h to remove  $\text{SiO}_2$ .

### 2.4. Synthesis of $\text{SnS}_{2-x}/\text{NHCS}$

NHCS (10 mg),  $\text{SnCl}_4 \cdot 0.5 \text{ H}_2\text{O}$  (100 mg) and thioacetamide (75 mg) were mixed in ethanol (60 mL) to form a uniform suspension. The suspension was transferred into a Teflon-lined autoclave (80 mL) and kept at  $160^\circ\text{C}$  for 12 h. After natural cooling to room temperature, the as-prepared  $\text{SnS}_2/\text{NHCS}$  was collected by centrifugation at 5000 rpm for 10 min and washed three times with DI water and ethanol, followed by vacuum drying at  $60^\circ\text{C}$  overnight.  $\text{SnS}_2/\text{NHCS}$  (100 mg) was placed in a quartz tube and heated to  $350^\circ\text{C}$  at a rate of  $10^\circ\text{C min}^{-1}$  in an atmosphere containing 10% hydrogen with 90 % argon for 2 h to fabricate  $\text{SnS}_{2-x}/\text{NHCS}$ .  $\text{SnS}_{2-x}$  was produced by using the similar synthesis procedure for  $\text{SnS}_{2-x}/\text{NHCS}$ , just without addition of NHCS.  $\text{SnS}_2$  was synthesized in the absence of NHCS in a pure argon atmosphere.

### 2.5. Characterization

Field emission scanning electron microscopy (SEM, ZEISS SUPRA55), field emission transmission electron microscope (TEM, JEOL JEM 2100F) and atomic force microscope (AFM, Bruker MultiMode8) were employed to characterize the morphology/thickness of the as-synthesized samples. X-ray diffraction (XRD, PANalytical X'Pert Pro), X-ray photoelectron spectroscopy (XPS, Thermo Fisher Scientific, ESCALAB250Xi), ultraviolet photo-electron spectroscopy (UPS, Thermo ESCALAB 250XI) and X-ray absorption near-edge spectroscopy (XANES) were used to analyze the composition, crystallization, chemical/band structure of the samples. Electron paramagnetic resonance (EPR, Bruker EMXplus) was applied to verify the S vacancy. Nuclear magnetic resonance ( $^1\text{H}$  NMR, Bruker ADVANCEIII 400 MHz) was utilized to quantify the carbonaceous products from the electrochemical reduction of  $\text{CO}_2$ .

### 2.6. Electrochemical measurement

Typically,  $\text{SnS}_{2-x}/\text{NHCS}$  (2 mg) and Nafion solution (5 wt%, 30  $\mu\text{L}$ ) were mixed in pure ethanol (2 mL) via ultrasonication to form a homogeneous ink. Then, spreading the ink (1 mL) evenly onto carbon paper ( $1 \times 1 \text{ cm}^2$ ) and followed by drying at  $60^\circ\text{C}$  overnight to obtain the working electrode.  $\text{SnS}_{2-x}$  and  $\text{SnS}_2$  working electrodes were prepared following the similar procedure, just replacing  $\text{SnS}_{2-x}/\text{NHCS}$  with the mixture of  $\text{SnS}_{2-x}$  or  $\text{SnS}_2$  (1.2 mg) and NHCS (0.8 mg). The mass ratio of  $\text{SnS}_{2-x}$  ( $\text{SnS}_2$ ) to NHCS was set resembling that of  $\text{SnS}_{2-x}/\text{NHCS}$ , which was deduced by dissolving  $\text{SnS}_{2-x}/\text{NHCS}$  (1 mg) in diluted hydrochloric acid and then centrifuging and quantifying the weight of NHCS. Platinum and Ag/AgCl electrodes (in saturated KCl solution) were used as the counter and reference electrode, respectively. The CO<sub>2</sub>RR performance was evaluated in an H-cell (separated by Nafion 115) containing  $\text{KHCO}_3$  electrolyte ( $0.5 \text{ mol L}^{-1}$ , 50 mL) under ambient conditions. All applied potentials in the measurements were against the Ag/AgCl electrode and converted to against RHE by the following equation:

$$E (\text{vs. RHE}) = E (\text{vs. Ag/AgCl}) + 0.21 \text{ V} + 0.0591 \times \text{pH}$$

## 3. Results and discussion

### 3.1. DFT calculations for $\text{SnS}_2$ -based catalysts

$\text{SnS}_2$  is known for its excellent electrocatalytic activity, especially weak bonding with hydrogen but strong affinity with oxygen, making it an ideal candidate for CO<sub>2</sub>RR [24]. Using DFT calculations, we first constructed a single-layer  $\text{SnS}_2$  (Fig. 1a and S1) and a  $\text{SnS}_{2-x}$  layer by introducing an S vacancy to the  $\text{SnS}_2$  layer (Fig. 1b and S2), respectively, to represent the single-component catalyst surface. Distinct from the case of  $\text{SnS}_2$  (Fig. S3), the charge density plot showed that electrons tend to aggregate around Sn atoms near the S vacancy in the  $\text{SnS}_{2-x}$  layer (Fig. 1c and S4). The electron localization function (ELF) mapping (Fig. S5) further confirmed that the presence of S vacancy changed the charge distribution on the surface of  $\text{SnS}_{2-x}$ . The ELF value of the regions between Sn and S was 0.3–0.4, suggesting a weak metallic-type interaction between Sn and S atoms [25]. Compared with  $\text{SnS}_2$ , the Sn atoms near the S vacancy in  $\text{SnS}_{2-x}$  became extra charge accumulation sites. Such site on the catalyst surface is beneficial to  $\text{CO}_2$  activation through effective bonding with the intermediates [13,16]. The band structure and density of states (DOS) of the  $\text{SnS}_2$  and  $\text{SnS}_{2-x}$  layer (Figs. 1d and 1e) showed that  $\text{SnS}_{2-x}$  had more energy levels near Fermi level ( $E_F$ ) compared with that of  $\text{SnS}_2$ , suggesting that S vacancy can urge more molecular orbitals to involve in the hybridization. Especially, a new defect level (marked by the grey rectangle) appeared near  $E_F$ , which modifies the surface electronic structure of the catalyst to benefit

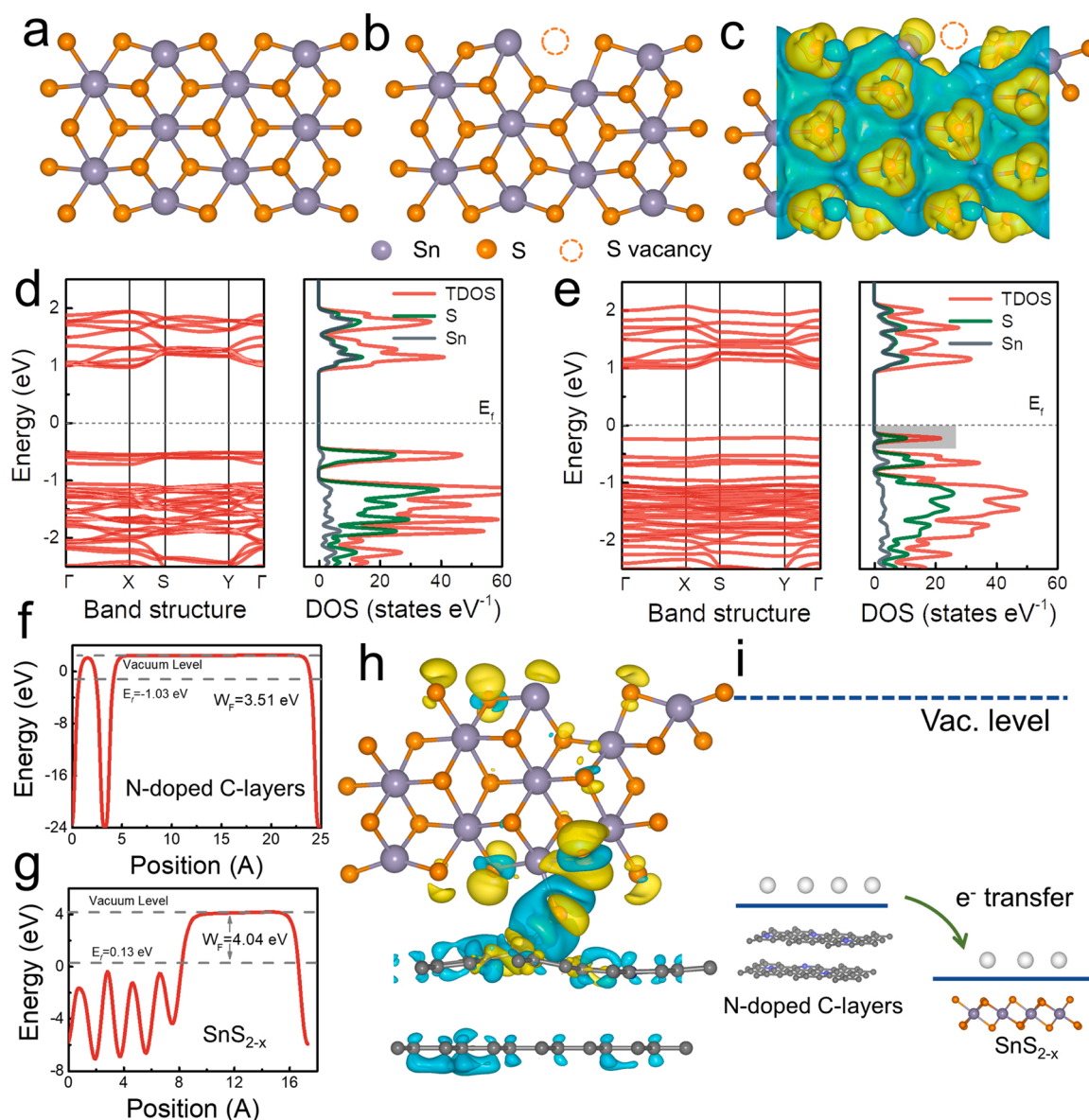


**Fig. 1.** DFT calculations for the electronic structure of  $\text{SnS}_2$  and  $\text{SnS}_{2-x}$  surface layer. DFT-optimized structural model of (a)  $\text{SnS}_2$  and (b)  $\text{SnS}_{2-x}$ . (c) Charge density difference diagram of the  $\text{SnS}_{2-x}$  layer, where the yellow and light green color represent electron accumulation and electron deletion, respectively; the isosurface value is  $0.003 \text{ e} \text{ \AA}^{-3}$ . Calculated band structure and the corresponding DOS of (d)  $\text{SnS}_2$  and (e)  $\text{SnS}_{2-x}$ . Work function of (f) NC and (g)  $\text{SnS}_{2-x}$ . (h) Charge density difference plot of  $\text{SnS}_{2-x}/\text{NC}$ , where the isosurface value is  $0.001 \text{ e} \text{ \AA}^{-3}$ . (i) Proposed scheme for the electron transfer from NC to  $\text{SnS}_{2-x}$ .

the exposure of the active sites for CO<sub>2</sub>RR [26].

It has been well addressed that a heterojunction constructed by two components with different work functions can induce the electron transfer from the one with lower work function to the other [27–29], and doping of N atoms can significantly reduce the work function of carbonaceous material [30]. We next established the model of N-doped carbon layers (NC, Fig. S6). The calculated work function of NC located at 3.51 eV (Fig. 1 f), which was lower than that of  $\text{SnS}_{2-x}$  (4.04 eV) and  $\text{SnS}_2$  (4.19 eV) (Fig. 1 g and S7). The results suggested that the coupling between NC and  $\text{SnS}_{2-x}$  (Fig. S8) would enable effective electron transfer from the former to the latter, which was confirmed by the charge density difference mapping of  $\text{SnS}_{2-x}/\text{NC}$  (Fig. 1 h). Based on these calculated results, S vacancy in the  $\text{SnS}_{2-x}$  surface layer and its chemical coupling with NC could promote the reduction activity of CO<sub>2</sub>, regulate the band structure and DOS of  $\text{SnS}_{2-x}$  hence the charge distribution and transfer, and enable electron flow from NC to  $\text{SnS}_{2-x}$  for CO<sub>2</sub>RR, as illustrated in Fig. 1i.

### 3.2. Synthesis and characterization of as-synthesized catalysts

Guided by the above-mentioned theoretical prediction, we synthesized  $\text{SnS}_{2-x}/\text{NHCS}$  by a procedural assembly as follows (Fig. 2a): silicon dioxide ( $\text{SiO}_2$ ) nanospheres with a diameter of  $\sim 200 \text{ nm}$  were first synthesized as sacrificial template by hydrolysis of TEOS (Fig. S9a); dopamine hydrochloride was then employed to form a conformal coating layer on the surface of  $\text{SiO}_2$  nanospheres under alkaline conditions (Fig. S9b); the dopamine layer converted to the N-doped carbon shell by pyrolysis at  $800^\circ\text{C}$  (Fig. S9c); NHCS was next obtained by etching  $\text{SiO}_2$  away (Fig. S9d); the hollow spheres of  $\text{SnS}_2/\text{NHCS}$  were finally assembled by the hydrothermal reaction of NHCS with Sn- and S-precursor to form the  $\text{SnS}_2$  layer on NHCS (Fig. S9e). S vacancies were deliberately introduced by thermal reaction with  $\text{H}_2$  to acquire  $\text{SnS}_{2-x}/\text{NHCS}$  (Fig. S9f).

TEM image revealed the typical hierarchical hollow structure of  $\text{SnS}_{2-x}/\text{NHCS}$ , where the spherical skeleton and the nearly transparent thin flakes equipped on the sphere were attributed to NHCS and  $\text{SnS}_{2-x}$ ,



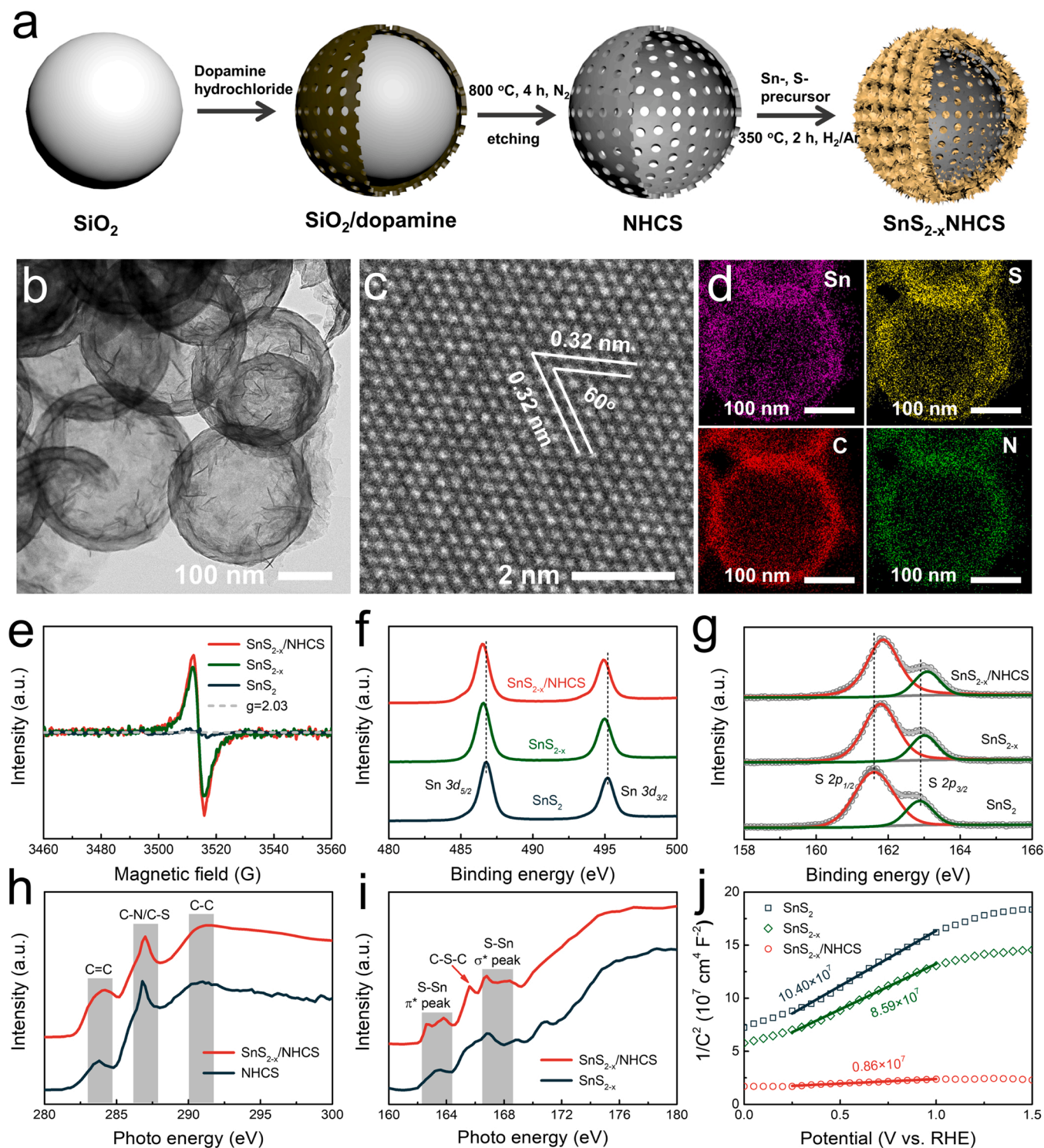


**Fig. 2.** Synthesis and characterization of  $\text{SnS}_{2-x}/\text{NHCS}$ . (a) Schematic illustration for the synthesis, (b) TEM, (c) HRTEM, and (d) elemental mapping images of  $\text{SnS}_{2-x}/\text{NHCS}$ . (e) EPR, (f) Sn 3d and (g) S 2p XPS spectra of  $\text{SnS}_2$ ,  $\text{SnS}_{2-x}$  and  $\text{SnS}_{2-x}/\text{NHCS}$ . (h) C K-edge XANES spectra of  $\text{SnS}_{2-x}/\text{NHCS}$  and  $\text{NHCS}$ ; (i) S L-edge XANES spectra of  $\text{SnS}_{2-x}/\text{NHCS}$  and  $\text{SnS}_{2-x}$ . (j) Mott-Schottky curves of  $\text{SnS}_2$ ,  $\text{SnS}_{2-x}$  and  $\text{SnS}_{2-x}/\text{NHCS}$ .

respectively (Fig. 2b). Compared with  $\text{SnS}_2$  and  $\text{SnS}_{2-x}$  (Fig. S10), the assembly of  $\text{SnS}_{2-x}$  flakes on the hollow spheres reduced the stacking of the  $\text{SnS}_{2-x}$  layers, which could benefit the exposure of their active sites for CO<sub>2</sub>RR. Based on the high-resolution (HR)-TEM images (Figs. S11 and 2c), whilst NHCS was amorphous, crystallinity of  $\text{SnS}_{2-x}$  was observed where the interplanar distance of two legible lattice fringes (0.32 nm) matched the (100) planes of hexagonal  $\text{SnS}_2$ . The energy-dispersive X-ray spectroscopy (EDX) mapping indicated the uniform

distribution of Sn, S, C and N elements over the  $\text{SnS}_{2-x}/\text{NHCS}$  hollow spheres (Fig. 2d). From the AFM image, the  $\text{SnS}_{2-x}$  flakes detached from  $\text{SnS}_{2-x}/\text{NHCS}$  had a typical thickness of  $\sim 1.6$  nm (Fig. S12). XRD patterns of the  $\text{SnS}_2$ ,  $\text{SnS}_{2-x}$  and  $\text{SnS}_{2-x}/\text{NHCS}$  samples showed similar diffraction peaks at  $14.8^\circ$ ,  $28.3^\circ$ ,  $32.3^\circ$ ,  $41.9^\circ$  and  $50.2^\circ$  (Fig. S13), corresponding to the (001), (100), (101), (102) and (110) planes of hexagonal  $\text{SnS}_2$  (JCPDS No. 23-0677), respectively; the amorphous NHCS did not contribute to the diffraction pattern noticeably.

We then employed EPR, XPS and XANES to semi-quantify the S vacancies, describe the coupling between  $\text{SnS}_{2-x}$  and NHCS, and further investigate the work function and carrier density by UPS and Mott-Schottky curve. Different from the EPR spectrum of  $\text{SnS}_2$  that showed no evident peak,  $\text{SnS}_{2-x}$  and  $\text{SnS}_{2-x}/\text{NHCS}$  exhibited a markedly enhanced signal at  $g = 2.03$  (Fig. 2e), indicating their much higher concentration of S vacancies than that in  $\text{SnS}_2$ . XPS survey confirmed the presence of Sn, S, N, C elements in  $\text{SnS}_{2-x}/\text{NHCS}$  (Fig. S14).  $\text{SnS}_2$  showed Sn  $3d_{5/2}$  and  $3d_{3/2}$  peaks at 486.6 and 450.1 eV (Fig. 2f) together with S  $2p_{3/2}$  and  $2p_{1/2}$  peaks at 161.6 and 162.8 eV (Fig. 2g), respectively; the samples involving  $\text{SnS}_{2-x}$  both showed blue shift for the Sn  $3d$  and red shift for S  $2p$  peaks. Such peak shifts primarily originated from the oxidized S and reduced Sn states compared with those for  $\text{SnS}_2$ , further evidencing the variation induced by S vacancies [31]. Compared with the spectra of  $\text{SnS}_{2-x}$ , the Sn  $3d$  and S  $2p$  peaks of  $\text{SnS}_{2-x}/\text{NHCS}$  slightly further blue shifted and red shifted, respectively, implying the coupling hence charge transfer between  $\text{SnS}_{2-x}$  and NHCS. Moreover, C  $1s$  peak of  $\text{SnS}_{2-x}/\text{NHCS}$  can be deconvoluted into multiple sub-peaks, where the one located at 286.5 eV corresponded to C–S bonding (Fig. S15) [32,33]. Additionally, for the XANES results, the C K-edge spectra of NHCS and  $\text{SnS}_{2-x}/\text{NHCS}$  (Fig. 2h) were dominated by three strong resonance signals centered at  $\sim 284.4$ , 286.8, and 291.2 eV, which were attributed to the dipole transition of C  $1s$  core electron into the  $\pi^* \text{C}=\text{C}$ ,  $\pi^* \text{C}-\text{O}/\text{N}-\text{S}-\text{C}$ , and  $\sigma^* \text{C}-\text{C}$  antibonding states, respectively [34,35]; L-edge spectra (Fig. 2i) of  $\text{SnS}_{2-x}$  and  $\text{SnS}_{2-x}/\text{NHCS}$  showed peaks in the region of 162.2–164.4 eV and 166.4–168.6 eV, corresponding to  $\pi^* \text{S}-\text{Sn}$  and  $\sigma^* \text{S}-\text{Sn}$ , respectively, while the peak at  $\sim 165.6$  eV of  $\text{SnS}_{2-x}/\text{NHCS}$  corresponded to the C–S–C coordination species [35,36]. These XPS and XANES results indicated the chemical bonding between NHCS and  $\text{SnS}_{2-x}$  in the hybrid. Fig. S16 showed the secondary electron cutoff measured by UPS: the work function of NHCS was 3.36 eV, which was lower than that of  $\text{SnS}_{2-x}$  (3.88 eV) and  $\text{SnS}_2$

(4.15 eV). As deduced from the slope of Mott-Schottky plots (Fig. 2j),  $\text{SnS}_{2-x}/\text{NHCS}$  delivered a high carrier density [37] which was 12.1 and 10.0 folds as that of  $\text{SnS}_2$  and  $\text{SnS}_{2-x}$ , which was primarily attributed to the  $E_F$  level difference between NHCS and  $\text{SnS}_{2-x}$  hence the convenient channel for electron flow. All the above-mentioned results confirmed that a hybrid hollow sphere with S vacancies was successfully constructed, showing effective chemical coupling between  $\text{SnS}_{2-x}$  and NHCS and the largely-enhanced carrier density.

### 3.3. CO2RR performance of as-synthesized catalysts

We measured the surface contact angle of  $\text{SnS}_2$ ,  $\text{SnS}_{2-x}$  and  $\text{SnS}_{2-x}/\text{NHCS}$  with respect to water before CO2RR (Fig. S17). All catalysts exhibited hydrophobicity, which facilitates gas capture on the catalyst surface and is beneficial to the  $\text{CO}_2$  adsorption at the electrode-solution interface and the reduction selectivity of CO2RR [38,39]. The CO2RR performance of  $\text{SnS}_{2-x}/\text{NHCS}$  was evaluated in an H-cell containing  $\text{CO}_2$ -saturated 0.5 mol  $\text{L}^{-1}$   $\text{KHCO}_3$  solution with a three-electrode system, where the performance of  $\text{SnS}_2$  and  $\text{SnS}_{2-x}$  were recorded as comparison. Prior to the CO2RR test, all the catalysts were first electrochemically activated by cyclic voltammetry measurement until stable characteristic curves were obtained [40]. The linear sweep voltammetry (LSV) curves of the samples were then measured at a scan rate of 10  $\text{mV s}^{-1}$  (Fig. S18):  $\text{SnS}_{2-x}/\text{NHCS}$  provided evidently higher current density than that of  $\text{SnS}_2$  and  $\text{SnS}_{2-x}$  at various applied potentials while  $\text{SnS}_{2-x}$  was better than  $\text{SnS}_2$ , implying the superiority of S vacancies and energy-level adapted junction via  $\text{SnS}_{2-x}$ -NHCS coupling. From the measured geometrical current density (Fig. 3a and S19),  $\text{SnS}_{2-x}/\text{NHCS}$  exhibited a predominant current density of  $35.3 \text{ mA cm}^{-2}$  at  $-1.2 \text{ V}$  (vs. RHE), which was 2.1 and 2.7 folds as that of  $\text{SnS}_{2-x}$  and  $\text{SnS}_2$ , respectively, suggesting that coupling with NHCS can effectively boost the current density. Specifically, the partial current density for formate

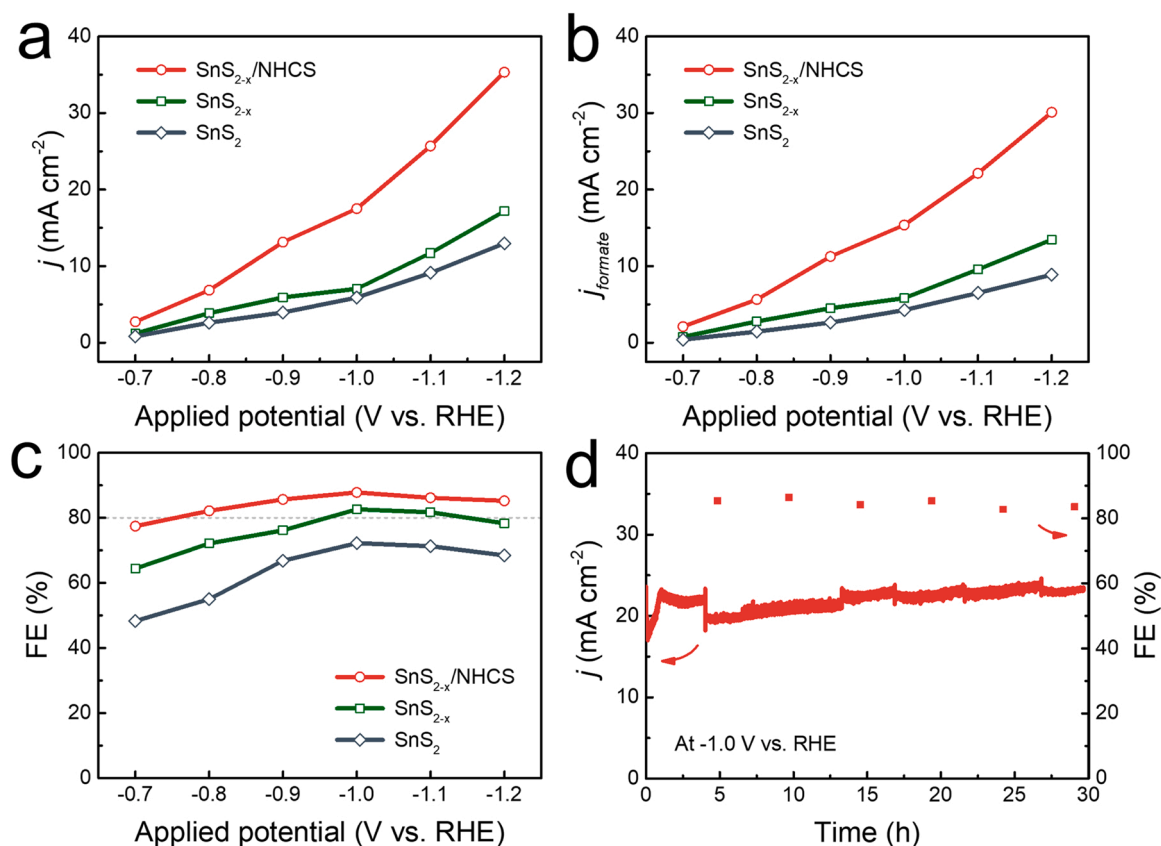


**Fig. 3.** Electrochemical CO2RR performance of  $\text{SnS}_{2-x}/\text{NHCS}$ . (a) Geometric current density, (b) partial current density for formate at various applied potentials, (c) FE of formate at various applied potentials catalyzed by  $\text{SnS}_2$ ,  $\text{SnS}_{2-x}$  and  $\text{SnS}_{2-x}/\text{NHCS}$ . (d) Durability evaluation of  $\text{SnS}_{2-x}/\text{NHCS}$  at  $-1.0 \text{ V}$  (vs. RHE) over 30 hrs.

( $j_{\text{formate}}$ , Fig. 3b) achieved from  $\text{SnS}_{2-x}/\text{NHCS}$  was  $30.1 \text{ mA cm}^{-2}$ , which was 2.2 and 3.4 folds as that of  $\text{SnS}_{2-x}$  and  $\text{SnS}_2$ , respectively. Moreover, for all these catalysts, the primary CO<sub>2</sub>RR carbonaceous product was formate (Fig. 3c, S20 and S21) with the maximum FE obtained at  $-1.0 \text{ V}$  (vs. RHE).  $\text{SnS}_{2-x}/\text{NHCS}$  showed the best product selectivity: FE of  $\text{SnS}_{2-x}/\text{NHCS}$ ,  $\text{SnS}_{2-x}$  and  $\text{SnS}_2$  was  $\sim 87.2\%$ ,  $82.6\%$  and  $72.2\%$  for formate conversion at  $-1.0 \text{ V}$  (vs. RHE), respectively. It was notable that, over a large potential range from  $-0.8 \text{ V}$  to  $-1.2 \text{ V}$  (vs. RHE),  $\text{SnS}_{2-x}/\text{NHCS}$  possessed  $> 80\%$  FE for formate and  $< 10\%$  FE for  $\text{H}_2$ . In comparison, the NHCS can only produce CO as the carbonaceous product accompanying with the generation of  $\text{H}_2$  (Fig. S22), where the reduction activity and selectivity for CO were both poor. Moreover,  $\text{SnS}_{2-x}/\text{NHCS}$  expressed a good durability upon 30 h continuous potentiostatic test at  $-1.0 \text{ V}$  (vs. RHE), showing no significant decay for CO<sub>2</sub>RR (Fig. 3d). After CO<sub>2</sub>RR operation, both XRD pattern (Fig. S23) and XP spectra (Fig. S24) showed barely any noticeable change, confirming the good stability of  $\text{SnS}_{2-x}/\text{NHCS}$ .

### 3.4. CO<sub>2</sub>RR enhancement mechanisms

To further uncover the critical factors for the CO<sub>2</sub>RR enhancement, we first measured the double-layer capacitance ( $C_{\text{dl}}$ ) to evaluate the

electrochemical active surface area (ECSA) of the catalysts, as  $C_{\text{dl}}$  is positively correlated with ECSA [41–43]. As presented in Fig. 4a and S25, the  $C_{\text{dl}}$  value increased from  $2.5 \text{ mF cm}^{-2}$  for  $\text{SnS}_2$  to  $3.0 \text{ mF cm}^{-2}$  for  $\text{SnS}_{2-x}$  and  $3.1 \text{ mF cm}^{-2}$  for  $\text{SnS}_{2-x}/\text{NHCS}$ . Apparently, the small increase of ECSA alone could not answer for the large CO<sub>2</sub> reduction enhancement. The geometrical current density at  $-0.9 \text{ V}$  (vs. RHE) was then plotted as a function of  $C_{\text{dl}}$  with different loading of  $\text{SnS}_2$ ,  $\text{SnS}_{2-x}$  and  $\text{SnS}_{2-x}/\text{NHCS}$  (Fig. 4b), showing a slope of 1.7, 3.0 and  $8.9 \text{ mA mF}^{-1}$ , respectively. The results indicated that the S vacancies and hybrid of NHCS and  $\text{SnS}_{2-x}$  were the major causes for the promotion of the CO<sub>2</sub>RR activity [44].

The prerequisite for CO<sub>2</sub>RR is the adsorption process of CO<sub>2</sub> molecules on the catalysts; high adsorption capacity and strong bonding with CO<sub>2</sub> are crucial for the consequent reaction(s) [45]. The measured adsorption isotherms (Fig. 4c) showed that  $\text{SnS}_{2-x}/\text{NHCS}$  had significantly superior CO<sub>2</sub> adsorption capacity over  $\text{SnS}_2$  and  $\text{SnS}_{2-x}$ . As the affinity to OH<sup>−</sup> can reflect the bonding strength with CO<sub>2</sub> [46], we conducted LSV measurement for OH<sup>−</sup> adsorption in N<sub>2</sub>-saturated  $0.5 \text{ mol L}^{-1}$  KOH electrolyte (Fig. 4d): similar to  $\text{SnS}_{2-x}/\text{NHCS}$ , the peaks of  $\text{SnS}_{2-x}$  located at lower voltages [0.32 and 0.11 V (vs. RHE)] compared with those of  $\text{SnS}_2$  [0.37 and 0.15 V (vs. RHE)], indicating that S vacancies in the samples could facilitate higher affinity to CO<sub>2</sub>.

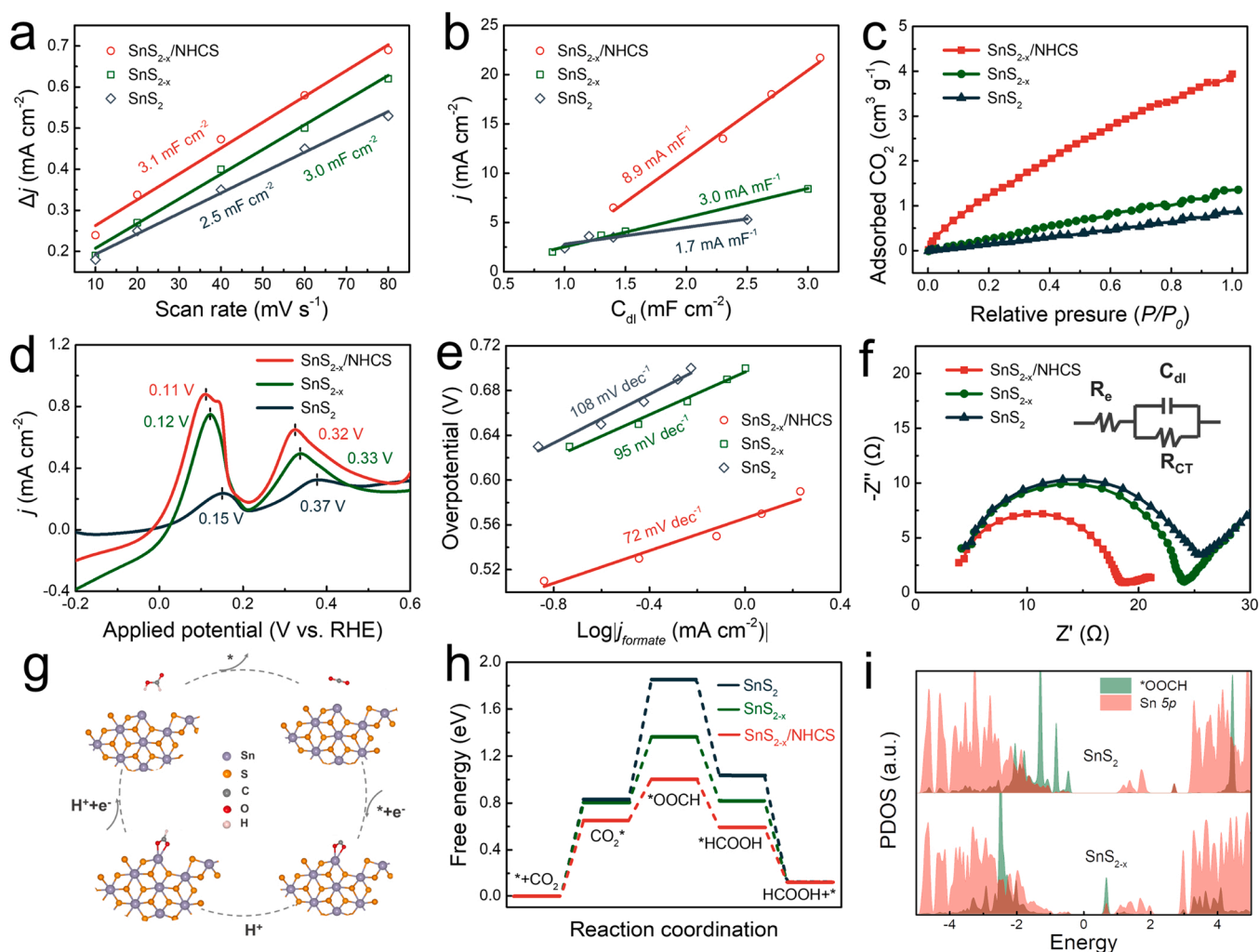


**Fig. 4.** Origin of CO<sub>2</sub>RR enhancement for  $\text{SnS}_{2-x}/\text{NHCS}$ . (a) Current density differences plotted as a function of scan rate (where the slope is twice the value of  $C_{\text{dl}}$ ), (b) geometrical current density at  $-1.0 \text{ V}$  (vs. RHE) plotted as a function of  $C_{\text{dl}}$  with different loading of the catalysts, (c) CO<sub>2</sub> adsorption isotherms, (d) OH<sup>−</sup> adsorption curves, (e) Tafel plots for  $\text{SnS}_2$ ,  $\text{SnS}_{2-x}$  and  $\text{SnS}_{2-x}/\text{NHCS}$ , (f) Nyquist plots of  $\text{SnS}_2$ ,  $\text{SnS}_{2-x}$  and  $\text{SnS}_{2-x}/\text{NHCS}$ . (g) Schematic diagram of CO<sub>2</sub>RR process at the S vacancy of  $\text{SnS}_{2-x}$ . (h) Calculated Gibbs free energy for formate production on  $\text{SnS}_2$ ,  $\text{SnS}_{2-x}$  and  $\text{SnS}_{2-x}/\text{NHCS}$ . (i) Calculated PDOS of \*OOCH and Sn 5p orbital for  $\text{SnS}_2$  and  $\text{SnS}_{2-x}$ , respectively.



Compared with SnS<sub>2</sub> and SnS<sub>2-x</sub>, the more powerful CO<sub>2</sub> adsorption capacity of SnS<sub>2-x</sub>/NHCS can contribute to the formation of a higher local CO<sub>2</sub> concentration, thus enhancing CO<sub>2</sub>RR to carbonaceous products rather than H<sub>2</sub> [12,45]. The Tafel slope of SnS<sub>2</sub>, SnS<sub>2-x</sub> and SnS<sub>2-x</sub>/NHCS (Fig. 4e) was 108, 95 and 72 mV dec<sup>-1</sup>, respectively. The results suggested that CO<sub>2</sub> activation was the major limitation step in the present case and a faster CO<sub>2</sub>RR kinetics can be achieved from SnS<sub>2-x</sub>/NHCS in comparison with SnS<sub>2</sub> and SnS<sub>2-x</sub> [47–50]. Moreover, Nyquist plots of the samples (Fig. 4f) demonstrated decreased electrical resistance of SnS<sub>2-x</sub>/NHCS, compared with that of SnS<sub>2</sub> and SnS<sub>2-x</sub>. Consistent with our theoretical analysis (Fig. 1) and the measured Mott-Schottky curve (Fig. 2j), the results further verified that S vacancies and chemical coupling of NHCS and SnS<sub>2-x</sub> could effectively benefit charge-transfer process.

It is known that the CO<sub>2</sub>RR process mainly involves four steps [12]: i) CO<sub>2</sub> molecule adsorbs on the active site of the catalysts; ii) activated CO<sub>2</sub> acquires H<sup>+</sup> to form the key intermediate \*OOCH; iii) \*OOCH combines with another H<sup>+</sup> to form HCOOH at the active site; iv) HCOOH desorbs and the active site is relegated (Fig. 4g). To further understand the origin of CO<sub>2</sub>RR enhancement in the present case, DFT calculations were carried out to simulate the reaction path on SnS<sub>2</sub>, SnS<sub>2-x</sub> and SnS<sub>2-x</sub>/NC surface (Figs. S26–28). Three states were proposed for each catalyst surface: i) the activated state representing CO<sub>2</sub> \* approaching the catalyst, ii) the transient state representing the formation of \*OOCH at the active site, and iii) the desorption state representing HCOOH\* near the catalyst surface [51]. At the transient state, the Sn–O bond length (*d*<sub>Sn–O</sub>) decreased from 2.40 Å for SnS<sub>2</sub> to 2.35 Å for SnS<sub>2-x</sub> and 2.30 Å for SnS<sub>2-x</sub>/NC; the shorter bond length indicated the enhanced bonding with the \*OOCH intermediate. Based on the calculated Gibbs free energy (Fig. 4h), the energy barrier for the formation of CO<sub>2</sub> \* on SnS<sub>2-x</sub>/NC surface was 0.65 eV, which was evidently lower than that on SnS<sub>2</sub> (0.83 eV) and SnS<sub>2-x</sub> (0.80 eV). Moreover, the energy barrier for the next step, i.e. the formation of \*OOCH, was 1.02, 0.56 and 0.36 eV on SnS<sub>2</sub>, SnS<sub>2-x</sub> and SnS<sub>2-x</sub>/NC, respectively. The significantly reduced energy barriers on SnS<sub>2-x</sub>/NC can effectively boost the CO<sub>2</sub> activation and conversion to formate, consistent with the promoted CO<sub>2</sub>RR observed experimentally. Furthermore, we projected the partial DOS (PDOS) of the calculated intermediate \*OOCH and Sn 5p (Fig. 4i): compared with the case of SnS<sub>2</sub>, the PDOS of \*OOCH overlapped more with Sn 5p for SnS<sub>2-x</sub>, supporting the stronger interaction of \*OOCH with SnS<sub>2-x</sub>. Moreover, the calculated charge density difference mapping (Fig. S29) revealed that more electrons aggregated towards \*OOCH adsorbed at the S vacancy, which is further beneficial to CO<sub>2</sub>RR.

#### 4. Conclusions

By introducing S vacancies to SnS<sub>2</sub> and chemical coupling SnS<sub>2-x</sub> with N-doped carbon, the hybrid SnS<sub>2-x</sub>/NHCS hollow sphere with distinct hierarchical structure delivered high current density (35.3 mA cm<sup>-2</sup> at –1.2 V vs. RHE) and high selectivity (FE > 80 % for formate) over a large potential range from –0.8 to –1.2 V (vs. RHE). Combining the experimental analysis with DFT calculations, we demonstrate that S vacancies induce additional charge accumulation sites meanwhile modify the charge distribution and band structure near the Fermi level, and the coupling with N-doped carbon constructs an efficient electron flow from NHCS to SnS<sub>2-x</sub> and further optimizes the electronic structure. The synergistic combination of S vacancies and energy-level adapted coupling of the hybrid increases the charge carrier density and conductivity, enhances the CO<sub>2</sub> adsorption capacity, strengthens affinity with the intermediate (\*OOCH), decreases the activation barrier for CO<sub>2</sub>RR, and accelerates the CO<sub>2</sub> reduction kinetics. The carrier density of SnS<sub>2-x</sub>/NHCS increases to 12.1 folds, and the partial current density and FE for formate increase to 3.4 and 1.2 folds, compared with that of SnS<sub>2</sub>. This work proposes not only a new electrocatalyst with high current density and product selectivity, but also an efficient strategy to boost the CO<sub>2</sub> activation capability and the

conductivity of electrocatalyst simultaneously by integration of vacancy engineering and matched energy-level structure of the hybrid.

#### CRedit authorship contribution statement

Yi Li: Conceptualization, Investigation, Writing – original draft preparation. Weidong Niu: Investigation. Tao Chen: Methodology, Characterization. Ye Sun: Writing – review & editing, Supervision, Funding acquisition. Miao Yu: Writing – review & editing, Supervision.

#### Declaration of Competing Interest

The authors declare that they have no known competing financial interests or personal relationships that could have appeared to influence the work reported in this paper.

#### Data Availability

Data will be made available on request.

#### Acknowledgment

This work was financially supported by the National Natural Science Foundation of China (51772066, 52073074), and State Key Laboratory of Urban Water Resource and Environment (2021TS08).

#### Appendix A. Supporting information

Supplementary data associated with this article can be found in the online version at doi:10.1016/j.apcatb.2022.122037.

#### References

- [1] G. Wang, J. Chen, Y. Ding, P. Cai, L. Yi, Y. Li, C. Tu, Y. Hou, Z. Wen, L. Dai, Electrocatalysis for CO<sub>2</sub> conversion: from fundamentals to value-added products, *Chem. Soc. Rev.* 50 (2021) 4993–5061.
- [2] S. Jin, Z.M. Hao, K. Zhang, Z.H. Yan, J. Chen, Advances and challenges for the electrochemical reduction of CO<sub>2</sub> to CO: from fundamentals to industrialization, *Angew. Chem., Int. Ed.* 60 (2021) 20627–20648.
- [3] A. Ozden, F.P.G. De Arquer, J.E. Huang, J. Wicks, J. Sisler, R.K. Miao, C.P. O'Brien, G. Lee, X. Wang, A.H. Ip, E.H. Sargent, D. Sinton, Carbon-efficient carbon dioxide electrolyzers, *Nat. Sustain.* 5 (2022) 563–573.
- [4] R.-B. Song, W. Zhu, J. Fu, Y. Chen, L. Liu, J.-R. Zhang, Y. Lin, J.-J. Zhu, Electrode materials engineering in electrocatalytic CO<sub>2</sub> reduction: energy input and conversion efficiency, *Adv. Mater.* 32 (2020) 1903796.
- [5] Z. Sun, T. Ma, H. Tao, Q. Fan, B. Han, Fundamentals and challenges of electrochemical CO<sub>2</sub> reduction using two-dimensional materials, *Chem* 3 (2017) 560–587.
- [6] J. Choi, J. Kim, P. Wagner, S. Gambhir, R. Jalili, S. Byun, S. Sayyar, Y.M. Lee, D. R. MacFarlane, G.G. Wallace, D.L. Officer, Energy efficient electrochemical reduction of CO<sub>2</sub> to CO using a three-dimensional porphyrin/graphene hydrogel, *Energy Environ. Sci.* 12 (2019) 747–755.
- [7] Y. Zou, S. Wang, An investigation of active sites for electrochemical CO<sub>2</sub> reduction reactions: from in situ characterization to rational design, *Adv. Sci.* 8 (2021) 2003579.
- [8] M. Zhu, P. Tian, X. Cao, J. Chen, T. Pu, B. Shi, J. Xu, J. Moon, Z. Wu, Y. Han, Vacancy engineering of the nickel-based catalysts for enhanced CO<sub>2</sub> methanation, *Appl. Catal. B Environ.* 282 (2021), 119561.
- [9] H. Han, S. Jin, S. Park, Y. Kim, D. Jang, M.H. Seo, W.B. Kim, Plasma-induced oxygen vacancies in amorphous MnO<sub>x</sub> boost catalytic performance for electrochemical CO<sub>2</sub> reduction, *Nano Energy* 79 (2021), 105492.
- [10] X. Cao, B. Wulan, B. Zhang, D. Tan, J. Zhang, Defect evolution of hierarchical SnO<sub>2</sub> aggregates for boosting CO<sub>2</sub> electrocatalytic reduction, *J. Mater. Chem. A* 9 (2021) 14741–14751.
- [11] B. Zhang, Y. Chang, Y. Wu, Z. Fan, P. Zhai, C. Wang, J. Gao, L. Sun, J. Hou, Regulating OCHO intermediate as rate-determining step of defective oxynitride nanosheets enabling robust CO<sub>2</sub> electroreduction, *Adv. Energy Mater.* 12 (2022) 2200321.
- [12] S. Gao, Z. Sun, W. Liu, X. Jiao, X. Zu, Q. Hu, Y. Sun, T. Yao, W. Zhang, S. Wei, Y. Xie, Atomic layer confined vacancies for atomic-level insights into carbon dioxide electroreduction, *Nat. Commun.* 8 (2017) 14503.
- [13] C. Peng, G. Luo, J. Zhang, M. Chen, Z. Wang, T. Sham, L. Zhang, Y. Li, G. Zheng, Double sulfur vacancies by lithium tuning enhance CO<sub>2</sub> electroreduction to n-propanol, *Nat. Commun.* 12 (2021) 1580.
- [14] J. Hu, L. Yu, J. Deng, Y. Wang, K. Cheng, C. Ma, Q. Zhang, W. Wen, S. Yu, Y. Pan, J. Yang, H. Ma, F. Qi, Y. Wang, Y. Zheng, M. Chen, R. Huang, S. Zhang, Z. Zhao,

- J. Mao, X. Meng, Q. Ji, G. Hou, X. Han, X. Bao, Y. Wang, D. Deng, Sulfur vacancy-rich MoS<sub>2</sub> as a catalyst for the hydrogenation of CO<sub>2</sub> to methanol, *Nat. Catal.* 4 (2021) 242–250.
- [15] T. Chen, T. Liu, X. Shen, W. Zhang, T. Ding, L. Wang, X. Liu, L. Cao, W. Zhu, Y. Li, T. Yao, Synergistically electronic tuning of metalloid CdSe nanorods for enhanced electrochemical CO<sub>2</sub> reduction, *Sci. China Mater.* 64 (2021) 2997–3006.
- [16] Z. Geng, X. Kong, W. Chen, H. Su, Y. Liu, F. Cai, G. Wang, J. Zeng, Oxygen vacancies in ZnO nanosheets enhance CO<sub>2</sub> electrochemical reduction to CO, *Angew. Chem. Int. Ed.* 57 (2018) 6054–6059.
- [17] J. Xu, X. Li, W. Liu, Y. Sun, Z. Ju, T. Yao, C. Wang, H. Ju, J. Zhu, S. Wei, Y. Xie, Carbon dioxide electroreduction into syngas boosted by a partially delocalized charge in molybdenum sulfide selenide alloy monolayers, *Angew. Chem. Int. Ed.* 56 (2017) 9121–9125.
- [18] F. Lei, W. Liu, Y. Sun, J. Xu, K. Liu, L. Liang, T. Yao, B. Pan, S. Wei, Y. Xie, Metallic tin quantum sheets confined in graphene toward high-efficiency carbon dioxide electroreduction, *Nat. Commun.* 7 (2016) 12697.
- [19] Z. Liu, L. Zeng, J. Yu, L. Yang, J. Zhang, X. Zhang, F. Han, L. Zhao, X. Li, H. Liu, W. Zhou, Charge redistribution of Ru nanoclusters on Co<sub>3</sub>O<sub>4</sub> porous nanowire via the oxygen regulation for enhanced hydrogen evolution reaction, *Nano Energy* 85 (2021), 105940.
- [20] R. He, X. Yuan, P. Shao, T. Duan, W. Zhu, Hybridization of defective tin disulfide nanosheets and silver nanowires enables efficient electrochemical reduction of CO<sub>2</sub> into formate and syngas, *Small* 15 (2019) 1904882.
- [21] N. Han, Y. Wang, L. Ma, J. Wen, J. Li, H. Zheng, K. Nie, X. Wang, F. Zhao, Y. Li, J. Fan, J. Zhong, T. Wu, D.J. Miller, J. Liu, S.-T. Lee, Y. Li, Supported cobalt polyphthalocyanine for high-performance electrocatalytic CO<sub>2</sub> reduction, *Chem* 3 (2017) 652–664.
- [22] C. Liu, W. Zhou, J. Zhang, Z. Chen, S. Liu, Y. Zhang, J. Yang, L. Xu, W. Hu, Y. Chen, Y. Deng, Air-assisted transient synthesis of metastable nickel oxide boosting alkaline fuel oxidation reaction, *Adv. Energy Mater.* 10 (2020) 2001397.
- [23] P. Kuang, Y. Wang, B. Zhu, F. Xia, C.-W. Tung, J. Wu, H. Chen, J. Yu, Pt Single atoms supported on N-doped mesoporous hollow carbon spheres with enhanced electrocatalytic H<sub>2</sub>-evolution activity, *Adv. Mater.* 33 (2021) 2008599.
- [24] A. Vasileff, C. Xu, Y. Jiao, Y. Zheng, S.-Z. Qiao, Surface and interface engineering in copper-based bimetallic materials for selective CO<sub>2</sub> electroreduction, *Chem* 4 (2018) 1809–1831.
- [25] P. Ravindran, P. Vajeeston, H. Fjellvåg, A. Kjekshus, Chemical-bonding and high-pressure studies on hydrogen-storage materials, *Comp. Mater. Sci.* 30 (2004) 349–357.
- [26] T. Chen, T. Liu, T. Ding, B. Pang, L. Wang, X. Liu, X. Shen, S. Wang, D. Wu, D. Liu, L. Cao, Q. Luo, W. Zhang, W. Zhu, T. Yao, Surface oxygen injection in tin disulfide nanosheets for efficient CO<sub>2</sub> electroreduction to formate and syngas, *Nano-Micro Lett.* 13 (2021) 189.
- [27] F. Xu, K. Meng, B. Cheng, S. Wang, J. Xu, J. Yu, Unique S-scheme heterojunctions in self-assembled TiO<sub>2</sub>/CsPbBr<sub>3</sub> hybrids for CO<sub>2</sub> photoreduction, *Nat. Commun.* 11 (2020) 4613.
- [28] C. Bie, B. Zhu, F. Xu, L. Zhang, J. Yu, In Situ grown monolayer n-doped graphene on CdS hollow spheres with seamless contact for photocatalytic CO<sub>2</sub> reduction, *Adv. Mater.* 31 (2019) 1902868.
- [29] P. He, L. Zhang, L. Wu, X. Yang, T. Chen, Y. Li, X. Yang, L. Zhu, Q. Meng, T. Duan, Synergistic effect of the sulfur vacancy and schottky heterojunction on photocatalytic uranium immobilization: the thermodynamics and kinetics, *Chem* 61 (2022) 2242–2250.
- [30] N. Yang, D. Yang, L. Chen, D. Liu, M. Cai, X. Fan, Design and adjustment of the graphene work function via size, modification, defects, and doping: a first-principle theory study, *Nanoscale Res. Lett.* 12 (2017) 642.
- [31] S. Yin, X. Zhao, E. Jiang, Y. Yan, P. Zhou, P. Huo, Boosting water decomposition by sulfur vacancies for efficient CO<sub>2</sub> photoreduction, *Energy Environ. Sci.* 15 (2022) 1556–1562.
- [32] G. Zou, H. Hou, C.W. Foster, C.E. Banks, T. Guo, Y. Jiang, Y. Zhang, X. Ji, Advanced hierarchical vesicular carbon co-doped with S, P, N for high-rate sodium storage, *Adv. Sci.* 5 (2018) 1800241.
- [33] G. Zhao, D. Yu, H. Zhang, F. Sun, J. Li, L. Zhu, L. Sun, M. Yu, F. Besenbacher, Y. Sun, Sulphur-doped carbon nanosheets derived from biomass as high-performance anode materials for sodium-ion batteries, *Nano Energy* 67 (2020), 104219.
- [34] Y. Zheng, Y. Jiao, Y. Zhu, L.H. Li, Y. Han, Y. Chen, A. Du, M. Jaroniec, S.Z. Qiao, Hydrogen evolution by a metal-free electrocatalyst, *Nat. Commun.* 5 (2014) 3783.
- [35] P. Chen, N. Zhang, S. Wang, T. Zhou, Y. Tong, C. Ao, W. Yan, L. Zhang, W. Chu, C. Wu, Y. Xie, Interfacial engineering of cobalt sulfide/graphene hybrids for highly efficient ammonia electrosynthesis, *Proc. Natl. Acad. Sci. U.S.A.* 116 (2019) 6635–6640.
- [36] Z. Jiang, W. Sun, H. Shang, W. Chen, T. Sun, H. Li, J. Dong, J. Zhou, Z. Li, Y. Wang, R. Cao, R. Sarangi, Z. Yang, D. Wang, J. Zhang, Y. Li, Atomic interface effect of a single atom copper catalyst for enhanced oxygen reduction reactions, *Energy Environ. Sci.* 12 (2019) 3508–3514.
- [37] Y. Li, G. Shi, T. Chen, L. Zhu, D. Yu, Y. Sun, F. Besenbacher, M. Yu, Simultaneous increase of conductivity, active sites and structural strain by nitrogen injection for high-yield CO<sub>2</sub> electro-hydrogenation to liquid fuel, *Appl. Catal. B Environ.* 305 (2022), 121080.
- [38] D. Wakerley, S. Lamaison, F. Ozanam, N. Menguy, D. Mercier, P. Marcus, M. Fontecave, V. Mougél, Bio-inspired hydrophobicity promotes CO<sub>2</sub> reduction on a Cu surface, *Nat. Mater.* 18 (2019) 1222–1227.
- [39] H.-Q. Liang, S. Zhao, X.-M. Hu, M. Ceccato, T. Skrydstrup, K. Daasbjerg, Hydrophobic copper interfaces boost electroreduction of carbon dioxide to ethylene in water, *ACS Catal.* 11 (2021) 958–966.
- [40] C.W. Lee, N.H. Cho, K.T. Nam, Y.J. Hwang, B.K. Min, Cyclic two-step electrolysis for stable electrochemical conversion of carbon dioxide to formate, *Nat. Commun.* 10 (2019) 3919.
- [41] G. Meng, T. Wei, W. Liu, W. Li, S. Zhang, W. Liu, Q. Liu, H. Bao, J. Luo, X. Liu, NiFe layered double hydroxide nanosheet array for high-efficiency electrocatalytic reduction of nitric oxide to ammonia, *Chem. Commun.* 58 (2022) 8097–8100.
- [42] D. Qi, F. Lv, T. Wei, M. Jin, G. Meng, S. Zhang, Q. Liu, W. Liu, D. Ma, M.S. Hamdy, J. Luo, X. Liu, High-efficiency electrocatalytic NO reduction to NH<sub>3</sub> by nanoporous VN, *Nano Res. Energy* 1 (2022), e9120022.
- [43] H. Zhang, Y. Qiu, S. Zhang, Q. Liu, J. Luo, X. Liu, Nitrogen-incorporated iron phosphosulfide nanosheets as efficient bifunctional electrocatalysts for energy-saving hydrogen evolution, *Ionics* 28 (2022) 3927–3934.
- [44] A. Zhang, R. He, H. Li, Y. Chen, T. Kong, K. Li, H. Ju, J. Zhu, W. Zhu, J. Zeng, Nickel Doping in atomically thin tin disulfide nanosheets enables highly efficient CO<sub>2</sub> reduction, *Angew. Chem. Int. Ed.* 57 (2018) 10954–10958.
- [45] G. Liu, Z. Li, J. Shi, K. Sun, Y. Ji, Z. Wang, Y. Qiu, Y. Liu, Z. Wang, P. Hu, Black reduced porous SnO<sub>2</sub> nanosheets for CO<sub>2</sub> electroreduction with high formate selectivity and low overpotential, *Appl. Catal. B Environ.* 260 (2020), 118134.
- [46] C. Dong, L. Cui, Y. Kong, C. Chen, H. Liu, Y. Zhang, W. Zhu, R. He, Elemental doping induced sulfur vacancies enable efficient electrochemical reduction of CO<sub>2</sub> over CdS nanorods, *J. Phys. Chem. C* 126 (2022) 102–109.
- [47] X. Wang, S. Liu, H. Zhang, S. Zhang, G. Meng, Q. Liu, Z. Sun, J. Luo, X. Liu, Polycrystalline SnS<sub>x</sub> nanofilm enables CO<sub>2</sub> electroreduction to formate with high current density, *Chem. Commun.* 58 (2022) 7654–7657.
- [48] M. Yang, J. Sun, Y. Qin, H. Yang, S. Zhang, X. Liu, J. Luo, Hollow CoFe-layered double hydroxide polyhedrons for highly efficient CO<sub>2</sub> electrolysis, *Sci. China Mater.* 65 (2022) 536–542.
- [49] S. Gao, T. Wei, J. Sun, Q. Liu, D. Ma, W. Liu, S. Zhang, J. Luo, X. Liu, Atomically dispersed metal-based catalysts for Zn-CO<sub>2</sub> batteries, *Small Struct.* (2022), <https://doi.org/10.1002/ssr.202200086>.
- [50] M. Jin, W. Liu, J. Sun, X. Wang, S. Zhang, J. Luo, X. Liu, Highly dispersed Ag clusters for active and stable hydrogen peroxide production, *Nano Res.* 15 (2022) 5842–5847.
- [51] X. Zhou, E. Song, Z. Kuang, Z. Gao, H. Zhao, J. Liu, S. Sun, C.-Y. Mou, H. Chen, Tuning selectivity of electrochemical reduction reaction of CO<sub>2</sub> by atomically dispersed Pt into SnO<sub>2</sub> nanoparticles, *Chem. Eng. J.* 430 (2022), 133035.